RSC Advances

PAPER

View Article Online
View Journal | View Issue

Cite this: *RSC Adv.*, 2021, **11**, 15905

Absorption and desorption of hydrogen in $Ti_{1.02}Cr_{1.1}Mn_{0.3}Fe_{0.6}RE_{0.03}$: experiments, characterization and analytical interpretation using statistical physics treatment

Fatma Aouaini, *[a] Nadia Bouazizi,[b] Maha M. Almoneef,*[a] Hanan Al-Ghamdi[a] and Abdelmottaleb Ben Lamine[b]

In this work, the absorption and desorption isotherms of hydrogen on $Ti_{1.02}Cr_{1.1}Mn_{0.3}Fe_{0.6}RE_{0.03}$ (RE = La, Ce, Ho) metals were collected at three temperatures under the same experimental conditions. This was carried out in order to determine the rare earth effect on the hydrogen storage performance of the $Ti_{1.02}Cr_{1.1}Mn_{0.3}Fe_{0.6}$ metal. The equilibrium data showing the hydrogen absorbed/released amounts per unit of absorbent mass have provided useful details to describe the absorption/desorption processes. Indeed, statistical physics formalism is appealing to ascribe advanced interpretations to the complexation mechanism. The physico-chemical parameters included in the model analytical expression are numerically determined from the experimental data fitting. We have found that the model can describe the complexation process through steric parameters such as the site densities (N_{1m} and N_{2m}), the numbers of atoms per site (n_1 and n_2) and energetic parameters (P_1 and P_2). The behavior of each parameter is examined in relation to the sorption mechanism. Overall, the energetic interpretation reveals that the desorption and absorption of H-gas in the $Ti_{1.02}Cr_{1.1}Mn_{0.3}Fe_{0.6}RE_{0.03}$ alloys can be characterized by chemical interactions. In addition, the expression of the appropriate model is exploited to determine the thermodynamic potential functions that describe the absorption phenomenon.

Received 5th February 2021
Accepted 15th April 2021

DOI: 10.1039/d1ra00999k

rsc.li/rsc-advances

1 Introduction

In search for solutions of alternative energies, hydrogen as a carrier of energy has become an important choice to resolve the issue of progressive exhausting fossil fuels and to safeguard the planet's environment, thanks to the renewability and purity of this gas.[1–4] Hydrogen storage has presented a basic problem for energy storage exploitation.[5] In general, hydrogen is stored as a cryogenic liquid, pressurized gas and chemically or physically related to the suitable solid-state matter.[5–8] Among these storage systems, solid-state storage methods depending on metal hydrides, which present high prospects for the great ability of H-storage in an efficient, compact, often reversible and quite safe manner; and, consequently, is progressively acquiring importance in applications for hydrogen storage.[9–12]

In particular, the Laves phases (AB_2) have been widely investigated owing to their great hydrogen storage performance, life cycle and good hydrogen absorption/desorption kinetics.[13,14] The A metal can be Zr, Ti or Mg, whereas the B metal can be V, Ni, Mn or Cr.[15] Amongst them, AB_2-type Ti–Cr-based metal as a type of hydrogen storage substance with elevated dehydrogenation pressure, great hydrogen storage capacity, exceptional anti-powdery characteristics and good kinetics is able to absorb or release hydrogen swiftly at room temperature and pressure.[16–20] Nevertheless, its hydrogen storage execution highly differs through the impact of metal constitution.[21] Consequently, a growing number of investigations have been concentrating on Ti–Cr-based solid solution metals in recent years. It is worth noting that the activation procedure is very necessary to use the hydrogen storage substances, as well as the mild activation condition, is favored. The Ti–Cr–Mn–Fe-based metal is difficult to be activated, which may be an obstruction for the practicable requests.

It is known that rare-earth alloys possess numerous activities. The addition of a few rare earth alloys in a TiFe metal that is hard to be activated leads to storing hydrogen readily.[22] Yan *et al.*[23] have discussed the impact of the rare earth Ce addition on the hydrogen storage characteristics and structure of $V_{55}Ti_{22.5}Cr_{16.1}Fe_{6.4}$. They discovered that, at room temperature, hydrogen can be absorbed rapidly in all Ce-containing metals. Wu *et al.*[24] also have deduced that RE added to $V_{55}Ti_{22.5}Cr_{16.1}Fe_{6.4}$ metal can ameliorate the absorption capacity rather than the activation property, plateau pressure and kinetics.

[a]*Department of Physics, College of Science, Princess Nourah Bint Abdulrahman University, Riyadh, Saudi Arabia. E-mail: fasaidi@pnu.edu.sa; mmalmoneef@pnu.edu.sa; Tel: +966 508675781*

[b]*Laboratory of Quantum and Statistical Physics, LR18ES18, Monastir University, Faculty of Sciences of Monastir, Tunisia*

Furthermore, Liu *et al.*[25] have reported that Ce additive ameliorates the flat appearance of the plateau.

Pressure–composition–temperature *P–C–T* curve is an efficient method to assess the efficiency of hydrogen storage alloys that are employed to analyze diverse qualities; among them, hydrogen plateau pressure of absorption/desorption process, hydrogen storage capacity, plateau slope, and hysteresis.[26–29] Furthermore, the thermodynamic parameters are also determined according to *P–C–T* curves at various temperatures.[30,31] However, with recurrent absorption/desorption of hydrogen, alterations in *P–C–T* isotherms takes place owing to the change in hydrogen storage characteristics, generally displayed through the reduction in reversible storage ability of hydrogen, rise in plateau slope and so on.[32,33]

Many researchers have studied hydrogen absorption/desorption isotherms by different models. The application of this method is significant to represent numerous microscopic characteristics.[34,35] Some of them are established using certain working hypotheses utilizing the treatment of statistical physics to depict the absorption/desorption phenomenon,[34,35] whereas others are purely empirical and have no microscopic or physical investigations.[36] To understand the absorption and desorption mechanisms of hydrogen, experimental studies are carried out and a theoretical study is performed to describe both of these processes.

The principal goals of this article are to evolve the activation characteristics of the metal by introducing RE components (La, Ce and Ho) in $Ti_{1.02}Cr_{1.1}Mn_{0.3}Fe_{0.6}$ metal and also to select a physical model which can analyze the physico-chemical characteristics of hydrogen absorption/desorption isotherms utilizing the grand canonical ensemble of the statistical physics approach. This modeling task is devoted to supplying new investigations at the molecular level. The density of active sites and the number of H-atoms per site have been assessed. The explanation of the alloy's performances by determining the absorbed and desorbed hydrogen quantities is revealed. The identification and description of the interaction type between hydrogen and absorbents have been clarified. Besides, the chosen model was used to calculate the thermodynamic potential functions during the absorption process.

2 Experimental study

2.1 Experimental procedure

The nominal composition of the studied alloys is represented by the following general formula: $Ti_{1.02}Cr_{1.1}Mn_{0.3}Fe_{0.6}RE_{0.03}$ (RE = La, Ce, Ho). The purity of all the raw materials utilized was at least 99%. The alloys were prepared in a water-cooled copper crucible under an argon atmosphere through induction levitation melting of the metallic components (overall weight of around 30 g). To achieve elevated homogeneity, the ingots were remelted three times.[37]

The crystal structures and lattice parameters of these metals were studied through X-ray diffraction (XRD) utilizing a Rigaku D/max-3B diffractometer with Cu Kα radiation.[37]

The properties of hydrogen storage of the substances were studied using a homemade Sieverts-type apparatus utilizing hydrogen with a purity of 99.99%. Before the measurement, the samples were preserved for 30 min under vacuum at 373 K and then, for activation, submitted to successive adsorption and desorption cycles of hydrogen at ambient temperature. The adsorption/desorption *P–C–T* isotherms of hydrogen were collected at T = 243, 253 and 263 K, and measured after an activation.[37]

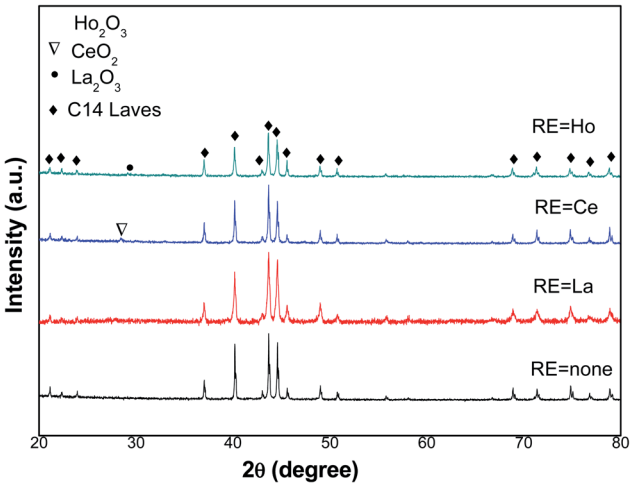

Fig. 1 XRD patterns of $Ti_{1.02}Cr_{1.1}Mn_{0.3}Fe_{0.6}RE_{0.03}$ alloys.

2.2 Experimental results

XRD patterns of the tested metals in the 2θ range of 20–80° are presented in Fig. 1. It is obvious that $Ti_{1.02}Cr_{1.1}Mn_{0.3}Fe_{0.6}$ metal presents one phase, which is the C14-type Laves structure, whereas the RE oxide phase is along with the C14-type Laves phase in metals containing RE. According to XRD analysis data, lattice parameters and cell volumes of all metals were determined and presented in Table 1.

We noticed that both lattice constants a and c of the C14 laves phase rise with the introduced RE additives. Consequently, the unit cell volume of $Ti_{1.02}Cr_{1.1}Mn_{0.3}Fe_{0.6}RE_{0.03}$ alloys increases too. As an example, the addition of La leads to its insertion in the unit cell of the absorbent to increase the dimensions of a, c, and consequently to its volume V, from 4.8543 Å, 7.9676 Å and 162.60 Å^3 for $Ti_{1.02}Cr_{1.1}Mn_{0.3}Fe_{0.6}$, and 4.8613 Å, 7.9726 Å and 163.16 Å^3 for $Ti_{1.02}Cr_{1.1}Mn_{0.3}Fe_{0.6}Ce_{0.03}$,

Table 1 The crystallographic data of $Ti_{1.02}Cr_{1.1}Mn_{0.3}Fe_{0.6}RE_{0.03}$ alloys

Alloys	Lattice parameters (10^{-1} nm)			Unit cell volume, V (10^{-3} nm^3)
	a	c	c/a	
$Ti_{1.02}Cr_{1.1}Mn_{0.3}Fe_{0.6}$	4.8543	7.9676	1.6413	162.60
$Ti_{1.02}Cr_{1.1}Mn_{0.3}Fe_{0.6}La_{0.03}$	4.8623	7.9746	1.6400	163.28
$Ti_{1.02}Cr_{1.1}Mn_{0.3}Fe_{0.6}Ce_{0.03}$	4.8613	7.9726	1.6400	163.16
$Ti_{1.02}Cr_{1.1}Mn_{0.3}Fe_{0.6}Ho_{0.03}$	4.8601	7.9710	1.6401	163.05

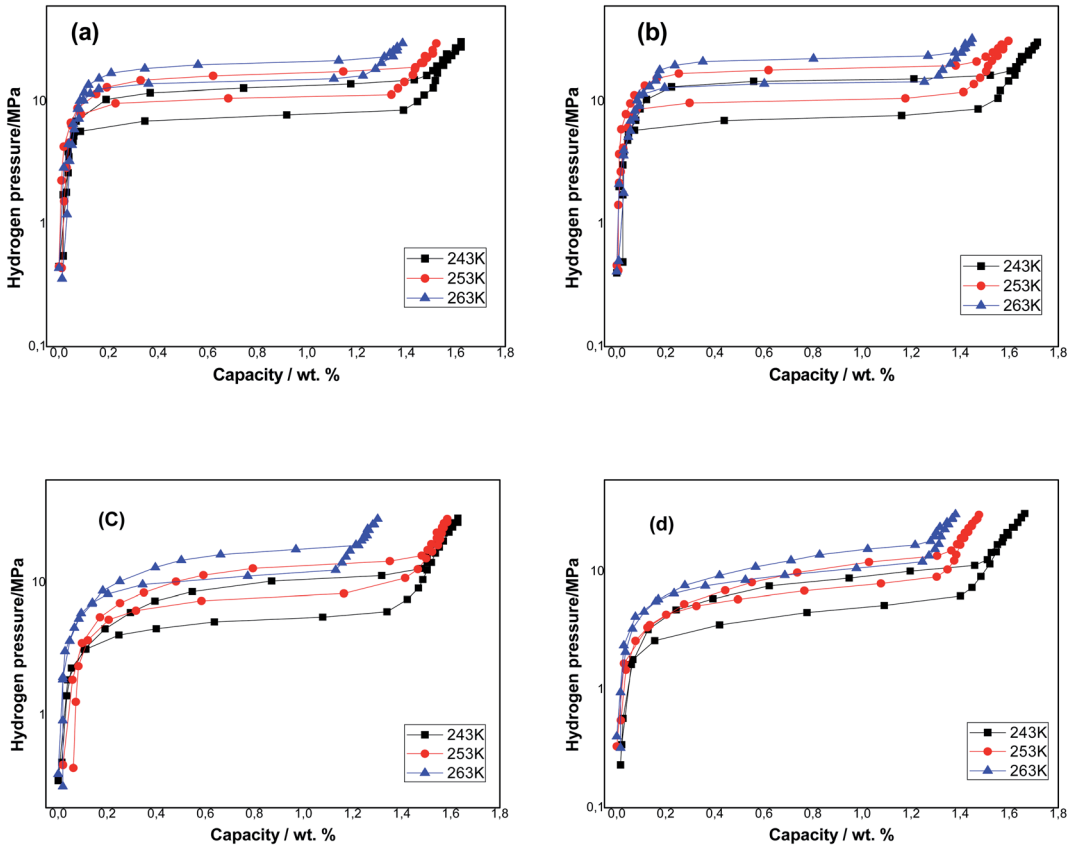

Fig. 2 *P–C–T* curves of $Ti_{1.02}Cr_{1.1}Mn_{0.3}Fe_{0.6}RE_{0.03}$ alloys: (a) $Ti_{1.02}Cr_{1.1}Mn_{0.3}Fe_{0.6}$ alloy; (b) $Ti_{1.02}Cr_{1.1}Mn_{0.3}Fe_{0.6}La_{0.03}$ alloy; (c) $Ti_{1.02}Cr_{1.1}Mn_{0.3}Fe_{0.6}Ce_{0.03}$ alloy; (d) $Ti_{1.02}Cr_{1.1}Mn_{0.3}Fe_{0.6}Ho_{0.03}$ alloy.

respectively. The lattice parameters of Ho and La containing alloys showed a similar change behavior.

The *P–C–T* isotherms of the samples obtained at three temperatures $T = 243$, 253 and 263 K are presented in Fig. 2, and the relative parameters of the absorption/desorption investigation are listed in Table 2. We noticed that each *P–C–T* curve has a single apparent plateau region. The plateau pressure of each sample rises with the rise of temperature. This is due to the low stabilization of hydrides at higher temperatures. The equilibrium pressures that are specified as the midpoints of absorption/desorption isotherms plateaus are listed in Table 2. As an example, the equilibrium pressure of the $Ti_{1.02}Cr_{1.1}Mn_{0.3}Fe_{0.6}$ sample was 7.59 MPa and that of the $Ti_{1.02}Cr_{1.1}Mn_{0.3}Fe_{0.6}La_{0.03}$ sample was 7.33 MPa at $T = 243$ K. After adding RE elements, the plateau pressure of the metals was reduced, which lead to a more stable hydride compared to $Ti_{1.02}Cr_{1.1}Mn_{0.3}Fe_{0.6}$ metal and the situation was identical for each tested temperature.

The sample's capacities reduce with the rise of temperature because of the exothermic proprieties of the hydrogen absorption reaction. The amount of hydrogen absorbed on all metals containing RE rise and the La additive-based metal attains the elevated quantity. After the addition of La, Ho and Ce respectively, hydrogen storage capacities rose from 1.621 wt% to 1.715 wt%, 1.663 wt% and 1.629 wt% at $T = 243$ K.

The hysteresis phenomenon was used to assess the pulverization resistance of the metals during the absorption/desorption phenomenon of hydrogen. In practical applications, a weak hysteresis is anticipated. The hysteresis of the samples is determined from the absorption/desorption

Table 2 The hydrogen storage characteristics of $Ti_{1.02}Cr_{1.1}Mn_{0.3}Fe_{0.6}RE_{0.03}$ (RE = La, Ce, Ho) metals

		P_{eq}^{abs} (MPa)			P_{eq}^{des} (MPa)			Hyst		
RE	C_{max} (wt%)	243 K	253 K	263 K	243 K	253 K	263 K	243 K	253 K	263 K
None	1.621	12.82	16.11	19.8	7.59	10.42	14.10	0.52	0.43	0.33
La	1.715	15.2	17.93	22.27	7.33	10.25	13.71	0.72	0.55	0.48
Ce	1.629	10.31	12.84	16.31	5.12	7.56	10.65	0.69	0.52	0.42
He	1.663	8.8	9.83	12.45	4.37	6.57	9.06	0.7	0.35	0.31

pressure at the plateau midpoint depending on the equation $\mathrm{Hys} = \ln(P_a/P_d)$. The results are presented in Table 2. It can be observed that $Ti_{1.02}Cr_{1.1}Mn_{0.3}Fe_{0.6}La_{0.03}$ metal presents the highest hysteresis factor equal to 0.72 at $T = 243$ K, while $Ti_{1.02}Cr_{1.1}Mn_{0.3}Fe_{0.6}Ho_{0.03}$ metal presents the smallest hysteresis factor of 0.31 at $T = 263$ K. The increase in temperature leads to the decrease of hysteresis of all alloys. It is well known that the increase in temperature has favorable effects on cycling stability and anti-pulverization ability.

3 Theoretical study: statistical physics analysis

3.1 Similarity between absorption and adsorption modeling

Absorption is the process, which occurs, when one substance penetrates the bulk or the volume of another substance, whereas adsorption occurs when one substance takes place on the surface of another substrate. Many studies have revealed that some statistical physics formalism can be similarly used for both adsorption and absorption[38] on account both mechanisms are related to the same category of diffusional equilibrium phenomenon.[37,39] Applying a mathematical study, Wjihi *et al.*[35,40] have revealed that the analytical adsorption model expressions were utilized to describe the absorption process too. As a result, the same models can be used to fit absorption isotherms in a manner similar to that performed for adsorption.

3.2 Statistical physics analysis

The application of statistical physics is a paramount procedure to study the absorption process since we can typify the considered system by determining the various physicochemical parameters implicated in the physical technique of absorption. The advantage of a statistical physics model is that it contains its analytical expression, significant parameters from a physical point of view, contrary to empirical models such as Langmuir and Freundlich,[41,42] in which the parameters do not have a direct physical meaning that we can derive from the measured isotherms after a numerical simulation.

The dissociation of the H_2 molecules at the contact of the substance results in atomically absorbed hydrogen. Thereafter, H gas is absorbed in the metal M and formed a metal hydride (MH) bulk where hydrogen atoms fill interstitial sites of the receptor substance. The overall reaction, arising during the sorption of hydrogen is, generally, represented through:[34,35]

$$\mathrm{M} + \frac{n}{2}\mathrm{H_2} \leftrightarrow \mathrm{MH}_n + \Delta Q \quad (1)$$

where the host anhydride substance is specified through M. The n parameter can be seen as a stoichiometric coefficient and H_n is defined as an aggregate of n atoms of hydrogen. ΔQ is the reaction heat of the absorption process.

In this work, as a first approach, the modeling is based on the following hypotheses: first, hydrogen is defined as a perfect gas because H_2 molecular interactions will be neglected.[43–45] Second, freedom internal degrees of hydrogen are neglected, excluding the translational degree and rotational degree which can be activated at room temperature. Finally, the utilization of the grand canonical partition function is required to investigate the absorption/desorption process.[43,46] This function for one interstitial site is formulated in the following general form:[46,47]

$$z_{gc} = \sum_{N_i} e^{-\beta(-\varepsilon_i - \mu)N_i} \quad (2)$$

where $(-\varepsilon)$ is the energy for one site, N_i is the interstitial site occupation state that adopts either the value 0 or 1, μ is the chemical potential of the site and $\beta = 1/k_B T$.

Considering that the sites are independent and identical. In this situation, the total grand canonical partition function of N_M identical sites has the form: $Z_{gc} = (z_{gc})^{N_M}$. Thereby, the expression of the average filled site number is determined using following equation[43,48]

$$N_0 = k_B T \frac{\partial \ln Z_{gc}}{\partial \mu} = N_M k_B T \frac{\partial \ln z_{gc}}{\partial \mu} \quad (3)$$

For the monolayer model with two energies, sorption is accomplished through two types of sites: some atoms are inserted in the first kind of site, whose energy is (ε_1) and defined by the density N_{1m}. We also assume that some atoms, which are inserted in the sites of type 2, whose energy is (ε_2), and are characterized by the density N_{2m}.

The total grand canonical partition function is determined by:

$$Z_{gc} = (z_{1gc})^{N_{1m}} (z_{2gc})^{N_{2m}} \quad (4)$$

The partial grand partition functions z_{1gc} and z_{2gc} have the following expressions:[35]

$$z_{1gc} = \sum_{N_i=0,1} e^{-\beta(-\varepsilon_1 - \mu)N_i} = 1 + e^{\beta(\varepsilon_1 + \mu)} \quad (5)$$

$$z_{2gc} = \sum_{N_i=0,1} e^{-\beta(-\varepsilon_2 - \mu)N_i} = 1 + e^{\beta(\varepsilon_2 + \mu)} \quad (6)$$

The formula associated with the diverse chemical potentials is defined by $\mu_m = \mu/n$ when the thermodynamic equilibrium is attained in eqn (1). μ is the host site chemical potential, μ_m is the H_2 molecule chemical potential and n is the number of atoms per site.

Based on the perfect gas estimation, the gaseous condition chemical potential is given as follows:[49]

$$\mu_m = k_B T \ln\left(\frac{N}{z_g}\right) \quad (7)$$

where

$$z_g = z_{gtr} \times z_{grot} = V\left(\frac{2\pi m k_B T}{h^2}\right) \times \frac{T}{2\theta_{rot}} \quad (8)$$

z_{gtr} is the translational partition function, z_{grot} is the rotational partition function, θ_{rot} is the conventional characteristic temperature of rotation for H_2 molecules, V is the volume of the

treated system, m is the H_2 gaseous molecule mass and h is Planck's constant.

The filled sites average number can be expressed as:[46]

$$N_0 = \frac{N_{1m}}{(1+e^{-\beta(\varepsilon_1+\mu)})} + \frac{N_{2m}}{(1+e^{-\beta(\varepsilon_2+\mu)})} \quad (9)$$

Based on the equilibrium state corresponding to the chemical potentials expressed by eqn (7), the filled sites average number represented by formula (9) turns to:[46]

$$N_0 = \frac{N_{1m}}{1+e^{-\beta\left(\varepsilon_{1m}+\mu_g\right)^{n_1}}} + \frac{N_{2m}}{1+e^{-\beta\left(\varepsilon_{2m}+\mu_g\right)}} = \frac{N_{1m}}{1+e^{(-\beta\varepsilon_{1m})^{n_1}}\left(\frac{z_g}{\beta P}\right)^{n_1}} + \frac{N_{2m}}{1+e^{(-\beta\varepsilon_{2m})^{n_2}}\left(\frac{z_g}{\beta P}\right)^{n_2}} \quad (10)$$

Assuming that $k_B T z_g e^{-\beta\varepsilon_m}$, we take a number of half-average filled sites $N_{01} = N_{1m}/2$ and $N_{02} = N_{2m}/2$ corresponding to the pressure at half-saturation defining the two types of sites, which is expressed as:[50,51]

$$P_1 = k_B T Z_g e^{-\beta\varepsilon_{1m}} \text{ and } P_2 = k_B T Z_g e^{-\beta\varepsilon_{2m}} \quad (11)$$

Thus, the filled sites average number has the relation as follow:

$$N_0 = N_{01} + N_{02} = \frac{N_{1m}}{1+\left(\frac{P_1}{P}\right)^{n_1}} + \frac{N_{2m}}{1+\left(\frac{P_2}{P}\right)^{n_2}} \quad (12)$$

Eqn (1) and the filled sites average number N_0 is used to find the average number of absorbed and released atoms:[52]

$$[H/M] = n_1 N_{01} + n_2 N_{02} \quad (13)$$

Finally, the relation corresponding to the hydrogen absorbed or released quantity is given by:[47]

$$[H/M] = [H/M]_1 + [H/M]_2 = \frac{n_1 N_{1m}}{1+\left(\frac{P_1}{P}\right)^{n_1}} + \frac{n_2 N_{2m}}{1+\left(\frac{P_2}{P}\right)^{n_2}} \quad (14)$$

For this model, the global eqn (1) could be divided into two simultaneous eqn (15) and (16):

$$M + \frac{n_1}{2}H_2 \rightarrow MH_{n_1} \quad (15)$$

and

$$M + \frac{n_2}{2}H_2 \rightarrow MH_{n_2} \quad (16)$$

We can then write the desorption equations as:

$$MH_{n_1'} \rightarrow M + \frac{n_1'}{2}H_2 \quad (17)$$

and

$$MH_{n_2'} \rightarrow M + \frac{n_2'}{2}H_2 \quad (18)$$

Since n_1' and n_2' are not necessarily identical to n_1 and n_2.

In the next part, we worked to specify the suitable model, which presents the best accordance with the measured data.

4 Modeling of experimental data using theoretical models

To select a suitable statistical physics model that presents the perfect adjustment with the measured absorption/desorption data, numerical software was used to fit the measured curves by four models (monolayer model with one, two and three energies and double-layer with two energies). This accurate adjusting technique depends on the Levenberg Marquardt iterating algorithm, which used a multivariable nonlinear regression program.

The two criteria employed, as indicators of the accuracy of the adjustment, are the multiple correlation coefficients squared R^2 and the residual root mean square error RMSE.[53,54] When the chosen model offers a great correlation with the absorption/desorption isotherms, the R^2 values must be close to 1 and the RMSE values must be near zero.

Table 3 Values of determination coefficient and the residual root mean square error (RMSE) for absorption mechanism

	$Ti_{1.02}Cr_{1.1}Mn_{0.3}Fe_{0.6}$			$Ti_{1.02}Cr_{1.1}Mn_{0.3}Fe_{0.6}La_{0.06}$			$Ti_{1.02}Cr_{1.1}Mn_{0.3}Fe_{0.6}Ce_{0.03}$			$Ti_{1.02}Cr_{1.1}Mn_{0.3}Fe_{0.6}Ho_{0.03}$		
T (K)	243 K	253 K	263 K	243 K	253 K	263 K	243 K	253 K	263 K	243 K	253 K	263 K
R^2												
Model 1	0.9953	0.9889	0.9821	0.9911	0.9928	0.9716	0.9809	0.9747	0.9712	0.9908	0.9892	0.9893
Model 2	**0.9993**	**0.9994**	**0.9983**	**0.9996**	**0.9998**	**0.9996**	**0.9986**	**0.9986**	**0.9972**	**0.9977**	**0.9986**	**0.9961**
Model 3	0.9950	0.9875	0.9971	0.9913	0.9961	0.9991	0.9894	0.9782	0.9660	0.9904	0.9841	0.9798
Model 4	0.9920	0.8157	0.9930	0.8209	0.8185	0.8186	0.9283	0.9213	0.9331	0.9465	0.9668	0.9634
RMSE												
Model 1	0.0343	0.0587	0.0908	0.0786	0.0544	0.1531	0.1305	0.1697	0.1151	0.0568	0.0496	0.0452
Model 2	**0.0039**	**0.0021**	**0.0066**	**0.0022**	**0.0007**	**0.0015**	**0.0075**	**0.0076**	**0.0085**	**0.0109**	**0.0053**	**0.0062**
Model 3	0.0218	0.0330	0.0087	0.0460	0.0177	0.0035	0.0454	0.3092	0.0777	0.0353	0.0418	0.0514
Model 4	0.0340	0.0912	0.0083	1.489	1.293	0.9213	0.4605	0.4959	0.2844	0.3081	0.1428	0.1449

Table 4 Values of determination coefficient and the residual root mean square error (RMSE) for desorption mechanism

	$Ti_{1.02}Cr_{1.1}Mn_{0.3}Fe_{0.6}$			$Ti_{1.02}Cr_{1.1}Mn_{0.3}Fe_{0.6}La_{0.03}$			$Ti_{1.02}Cr_{1.1}Mn_{0.3}Fe_{0.6}Ce_{0.03}$			$Ti_{1.02}Cr_{1.1}Mn_{0.3}Fe_{0.6}Ho_{0.03}$		
T (K)	243 K	253 K	263 K	243 K	253 K	263 K	243 K	253 K	263 K	243 K	253 K	263 K
R^2												
Model 1	0.9947	0.9918	0.9870	0.9942	0.9963	0.9878	0.9898	0.9891	0.9899	0.9952	0.9945	0.9934
Model 2	**0.9991**	**0.9988**	**0.9995**	**0.9997**	**0.9999**	**0.9992**	**0.9970**	**0.9965**	**0.9984**	**0.9982**	**0.9984**	**0.9983**
Model 3	0.9918	0.9878	0.9783	0.9904	0.9925	0.9842	0.9957	0.9903	0.9844	0.9928	0.9968	0.9755
Model 4	0.8529	0.7971	0.8123	0.9943	0.8130	0.7917	0.9926	0.9194	0.9028	0.9472	0.9246	0.9233
RMSE												
Model 1	0.0445	0.0535	0.0706	0.0464	0.0397	0.0829	0.0752	0.0719	0.0544	0.0306	0.0351	0.0369
Model 2	**0.0078**	**0.0058**	**0.0017**	**0.0014**	**0.0004**	**0.0041**	**0.0181**	**0.0078**	**0.0078**	**0.0099**	**0.0081**	**0.0076**
Model 3	0.0445	0.0451	0.0706	0.0465	0.0397	0.0670	0.0210	0.0381	0.0544	0.0275	0.0111	0.0892
Model 4	0.1167	0.1329	0.1137	0.0430	1.489	1.331	0.0518	0.4981	0.954	0.3143	0.4013	0.4059

For all the treated samples, RMSE and R^2 values utilizing a numerical simulation with the four statistical models are illustrated in Tables 3 and 4.

It is clear that the monolayer model with two energies is the most appropriate model to use in order to analyze the hydrogen isotherms of the tested samples for both phenomena at three temperatures. This model presented the greatest values of R^2 (R^2 > 0.9965) and the lowest values of RMSE (RMSE< 0.009) compared to the other models. In addition, the model parameters can be consistently evaluated. Therefore, it is possible to discuss and interpret the physicochemical interactions with hydrogen–alloy at a molecular level.

In the case of our samples, which belong to the C14 structure, many reports have revealed three types of tetrahedral sites

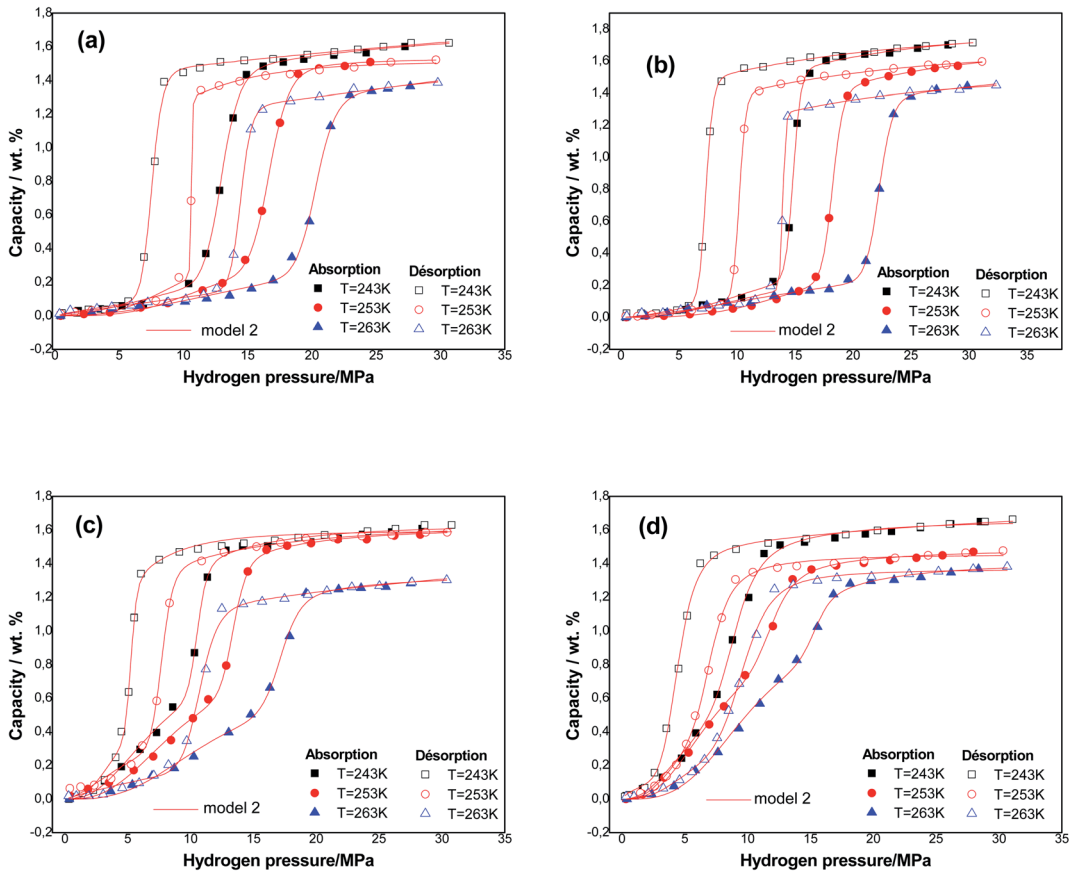

Fig. 3 Experimental absorption/desorption isotherms of hydrogen (dots) fitted by statistical model (continuous lines) at various temperatures of $Ti_{1.02}Cr_{1.1}Mn_{0.3}Fe_{0.6}RE_{0.03}$ alloys: (a) $Ti_{1.02}Cr_{1.1}Mn_{0.3}Fe_{0.6}$ alloy (b) $Ti_{1.02}Cr_{1.1}Mn_{0.3}Fe_{0.6}La_{0.03}$ alloy; (c) $Ti_{1.02}Cr_{1.1}Mn_{0.3}Fe_{0.6}Ce_{0.03}$ alloy; (d) $Ti_{1.02}Cr_{1.1}Mn_{0.3}Fe_{0.6}Ho_{0.03}$ alloy.

Table 5 Adjustment parameter values for absorption mechanism corresponding to the best-fitting model (model 2)

System	T (K)	n_1	n_2	N_{1m}	N_{2m}	P_1	P_2	$[H/M]_{1sat}$	$[H/M]_{2sat}$	$[H/M]_{sat}$
$Ti_{1.02}Cr_{1.1}Mn_{0.3}Fe_{0.6}$	243 K	1.56	18.88	0.274	0.065	12.97	15.21	0.42	1.227	1.65
	253 K	2.54	22.86	0.152	0.053	13.46	16.7	0.385	1.211	1.597
	263 K	1.84	27.15	0.2	0.038	18.68	20.31	0.368	1.03	1.39
$Ti_{1.02}Cr_{1.1}Mn_{0.3}Fe_{0.6}La_{0.06}$	243 K	1.335	28.38	0.3	0.048	14.81	21.24	0.4	1.36	1.76
	253 K	2.34	30.4	0.162	0.041	17.26	19.6	0.38	1.24	1.62
	263 K	1.64	31.52	0.21	0.0355	18.35	22.27	0.34	1.11	1.45
$Ti_{1.02}Cr_{1.1}Mn_{0.3}Fe_{0.6}Ce_{0.06}$	243 K	1.49	27.73	0.344	0.042	7.41	10.53	0.51	1.16	1.67
	253 K	1.77	28.86	0.28	0.037	9.06	13.4	0.49	0.95	1.44
	263 K	2.01	22.3	0.219	0.029	11.38	17.19	0.44	0.64	1.28
$Ti_{1.02}Cr_{1.1}Mn_{0.3}Fe_{0.6}Ho_{0.06}$	243 K	1.28	9.65	0.35	0.128	6.48	8.92	0.448	1.23	1.68
	253 K	1.42	13	0.31	0.08	7.16	11.83	0.44	1.04	1.48
	263 K	1.92	13.19	0.196	0.04	10.24	15.36	0.37	0.92	1.32

such as $[A_2B_2]$, $[B_4]$ and $[AB_3]$ sites for hydrogen absorption.[55,56] Many researchers using the density functional theory (DFT) showed that the most beneficial of these sites are the $[A_2B_2]$ sites pursued by $[AB_3]$ sites and the narrowest $[B_4]$ sites stay vacant.[57,58] Therefore, we deduce that in the C14-type Laves phase hydrogen mostly occupies two kinds of receptor sites: $[AB_3]$ and $[A_2B_2]$.[59] Thus, the apparition of two phases (α and β) during the absorption/desorption phenomenon of hydrogen proves that the two levels of energies are revealed in the chosen model.

Fig. 3 presents the experimental curves of alloys simulated utilizing the best fitting model at three temperatures.

The absorption and desorption processes are well described. It is valuable to enrich this point with an energetic and steric interpretation of both of these processes.

5 Results and discussions

The exploitation of the numerical simulations was performed by proposing the next investigations of the parameters, deduced, through an adjustment process using the ideal-fitting model. The fitting parameters are classified as follows: the first category contains the steric parameters as n_1 and n_2 numbers of H-atoms per site, N_{1m} and N_{2m} densities of interstitial sites and $[H/M]_{1sat}$ and $[H/M]_{2sat}$ the absorbed/desorbed quantities at saturation. The second category contains the energetic parameters as the half-saturation pressures P_1 and P_2 that reveal the hydrogen absorption/desorption energies in the tested metals. The analysis of these parameters is done by interpreting their behaviors as a function of temperature. Tables 5 and 6 show the values of the adjusted parameters for the absorption/desorption process, respectively.

5.1 Stereographic parameters

n_i and $n_1^{'}$ ($i = 1, 2$) are stoichiometric coefficients that represent the number of absorbed or released atoms per site, respectively. This parameter can also be considered as a steric coefficient, which can describe how H-atoms are inserted or dis-inserted in the host sites.

According to Tables 5 and 6, it can be seen that the number of absorbed/desorbed atoms per site, n_1 and n_2 is superior to 1 for all different temperatures and for all the studied alloys except for $Ti_{1.02}Cr_{1.1}Mn_{0.3}Fe_{0.6}Ho_{0.03}$ alloy where $n_2^{'} = 0.84 < 1$ at $T = 243$ K. This means that the hydrogen absorption expects in this case, is occurring in a multi-atom manner where more than one atom is inserted per site. As an example, for hydrogen absorption on $Ti_{1.02}Cr_{1.1}Mn_{0.3}Fe_{0.6}La_{0.03}$ at $T = 243$ K, $n_1 = 1.56$. First of all, we can notice that all the n_i adjusted values are not

Table 6 Adjustment parameter values for desorption mechanism corresponding to the best-fitting model (model 2)

System	T (K)	n_1	n_2	N_{1m}	N_{2m}	P_1	P_2	$[H/M]_{1sat}$	$[H/M]_{2sat}$	$[H/M]_{sat}$
$Ti_{1.02}Cr_{1.1}Mn_{0.3}Fe_{0.6}$	243 K	1.45	17.32	0.26	0.026	7.54	13.82	0.377	1.07	1.45
	253 K	1.31	20.19	0.23	0.05	10.64	16.1	0.3	1	1.3
	263 K	1.16	24.8	0.21	0.04	14.46	17.28	0.24	0.98	1.22
$Ti_{1.02}Cr_{1.1}Mn_{0.3}Fe_{0.6}La_{0.06}$	243 K	1.24	24.33	0.257	0.05	7.31	16.28	0.318	1.21	1.52
	253 K	2.07	27.84	0.15	0.039	10.19	16.6	0.31	1.08	1.39
	263 K	1.46	28	0.19	0.037	13.94	16.8	0.27	1.03	1.3
$Ti_{1.02}Cr_{1.1}Mn_{0.3}Fe_{0.6}Ce_{0.06}$	243 K	1.22	21.8	0.25	0.051	4.96	5.79	0.3	1.11	1.41
	253 K	1.12	17.93	0.21	0.057	5.7	7.36	0.23	1.02	1.25
	263 K	1.08	15.82	0.2	0.06	9.8	11	0.21	0.94	1.15
$Ti_{1.02}Cr_{1.1}Mn_{0.3}Fe_{0.6}Ho_{0.06}$	243 K	084	6.44	0.53	0.17	4.46	5.28	0.44	0.9	1.34
	253 K	1.35	9.3	0.22	0.09	5.41	7.01	0.29	0.837	1.12
	263 K	1.62	10.21	0.16	0.081	6.77	9.65	0.25	0.82	1.07

integers although they should be integers since the H-atom is indivisible. So, we can attribute the calculated non-integer values to an average value of a multitude of integer values. So, it is simple to describe this value ($n_1 = 1.56$) at minimum two integers. Since $1 < n < 2$, this expresses that the H-atoms are absorbed either by one or by two atoms per site with proportions x and $(1 - x)$, respectively. Then, we can write the following equation: $x \times 1 + (1 - x) \times 2 = 1.56$. This reveals that 44% of sites are inserted by one H-atom and 56% are inserted by two H-atoms. The variation of n_1 and n_2 in all the studied alloys in the absorption or desorption process *versus* temperature is given in Fig. 4. It was observed that for all the tested metals, n_1 was slightly constant with temperature. As we will see later, absorbed/desorbed energies for the first type of site α, which are greater compared to the second type β, explain this constant behavior. n_1 varies between 1.49 and 2.01 for $Ti_{1.02}Cr_{1.1}Mn_{0.3}Fe_{0.6}Ce_{0.03}$ sample as an example. The values of n_1 for all metals are lower than those for n_2, which is attributed to the narrow volume of α sites and their relatively high energies.

On the other hand, the values of n_2 are between 13 and 31 in the absorption process that means that the dynamics of H_2 molecules exchange and the capacity of hydrogen uptake of the β sites are higher than that of α sites. Therefore, we conclude that the size of the second insertion sites is superior to the first type of site.

For $Ti_{1.02}Cr_{1.1}Mn_{0.3}Fe_{0.6}RE_{0.03}$ (RE = La, Ho) metals, n_2 rises with the increase of temperature. This behavior is a property of an endothermic aggregation of H-atoms catalyzed by the presence of metallic interstices. However, for the other alloy $Ti_{1.02}Cr_{1.1}Mn_{0.3}Fe_{0.6}Ce_{0.03}$, n_2 first increases due to the endothermicity of the aggregation process. Then, it decreases at $T =$ 263 K due to the thermal agitation, which governs and leads to the destruction of the aggregate.

Comparing the values of this parameter during absorption and desorption processes, we can observe that n_1' and n_2' are respectively inferior to n_1 and n_2 for hysteresis causes and matter conservation since hydrogen atoms are deliberated with difficulty. Thus, the same α or β site will be emptied with lower numbers of hydrogen atoms n_1' and n_2'. In desorption with a lower dis-anchorage during α and β phases, the quantities of H-atoms $(n_1 - n_1')$ and $(n_2 - n_2')$ are preserved by the site, which reveals the existence of the hysteresis process in the isotherm desorption curves of hydrogen in all substances.

The host site densities N_{1m} and N_{2m} are also steric parameters correlated with the effectively inserted interstitial sites at saturation. Returning to the evolution of these parameters during the absorption/desorption process presented in Fig. 5, a decrease of these parameters is noticed in most cases with the temperature though slightly for N_{1m}. They generally change in the opposite way of n_1 and n_2. This opposite change of densities faces to n_1 and n_2 indicates an antagonistic effect, which is inflicted through the invariance of space volume. As for the decrease in N_{im}, it can be attributed to the classical thermal agitation. It can also be due to the existence of structural defects, which can intensely influence the hydrogen absorption

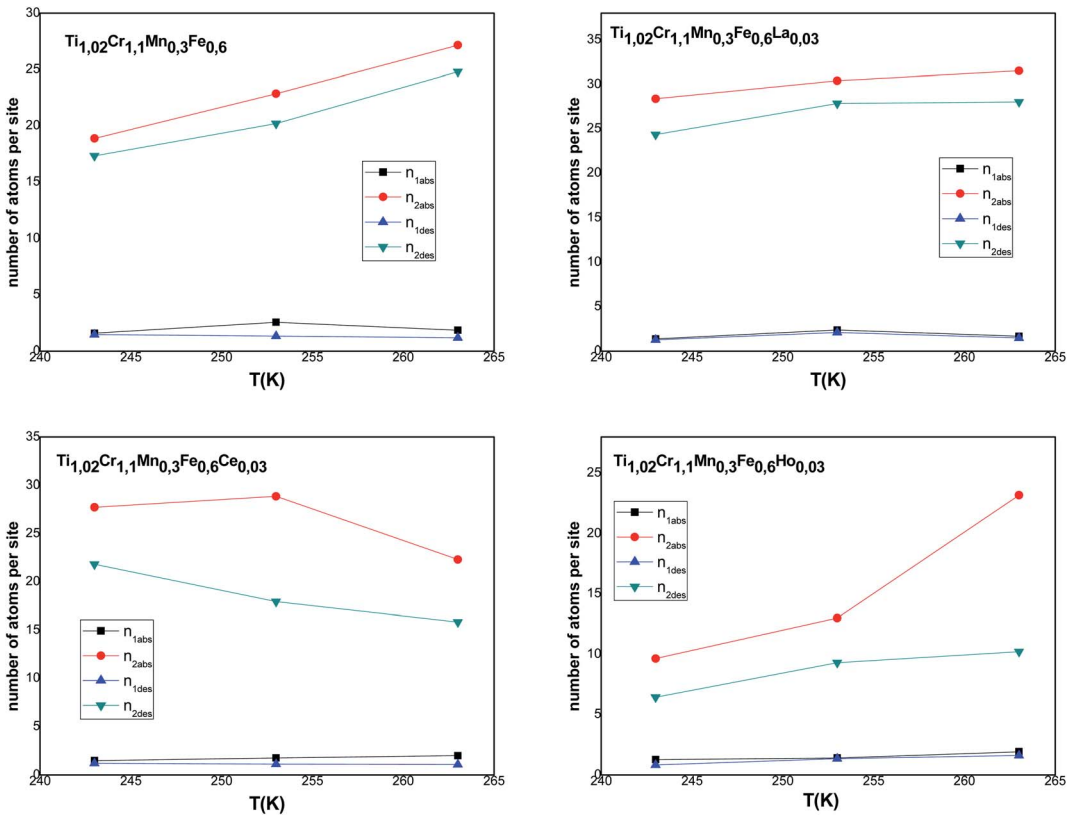

Fig. 4 Evolution of the number of atoms per site in absorption and desorption according to the temperature.

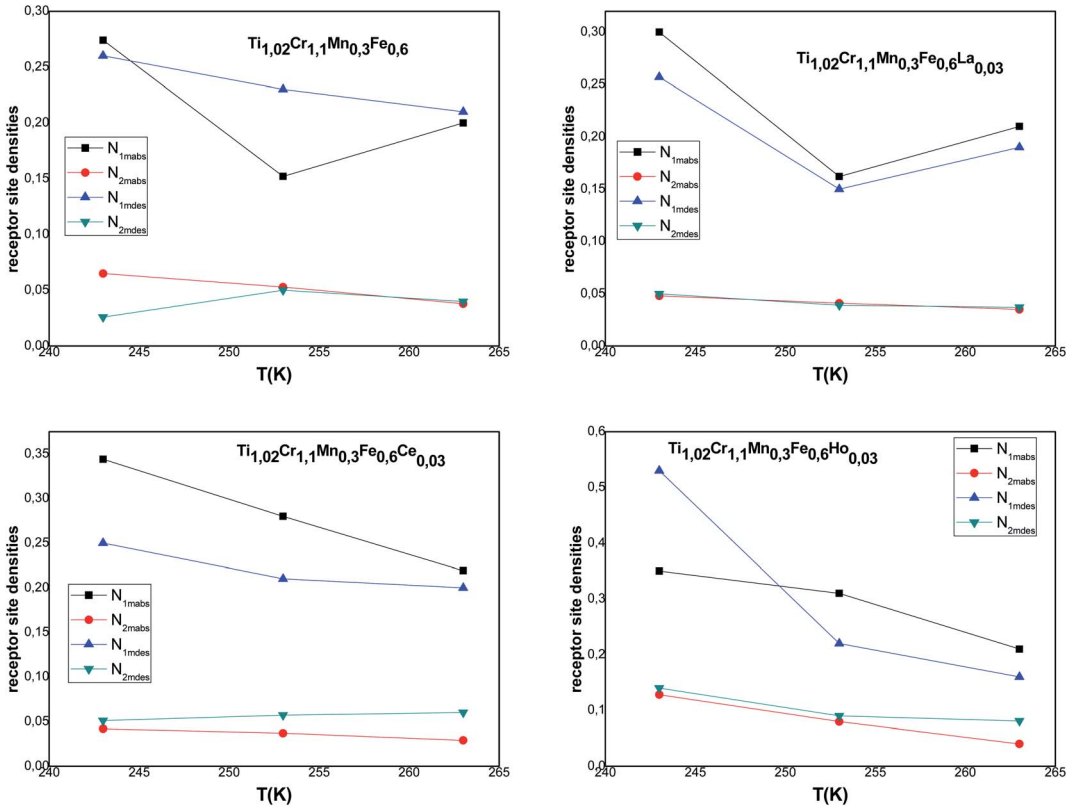

Fig. 5 Evolution of the interstitial site densities in absorption and desorption according to the temperature.

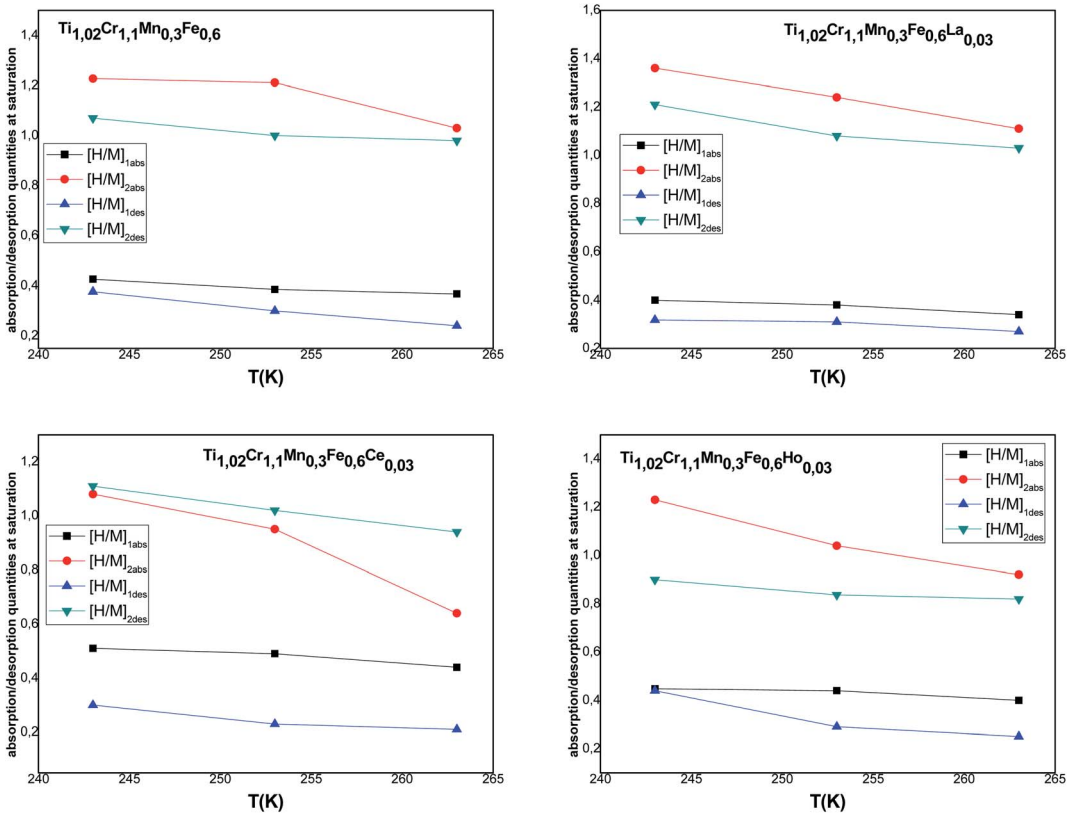

Fig. 6 Evolution of the monolayer absorbed/released quantities according to the temperature.

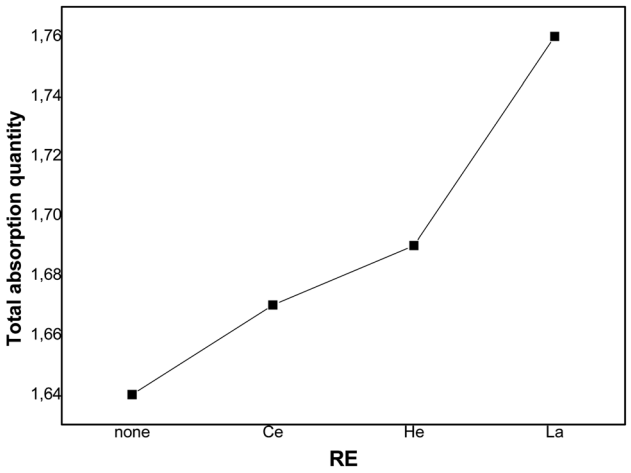

Fig. 7 Total quantity absorbed for different rare earth components.

process. Thus, the absorption of impurities in the volume can arise from both blocking of some receptor sites.

$[H/M]_{1sat} = n_1N_{1m}$ and $[H/M]_{2sat} = n_2N_{2m}$ are the capacity during both processes for α and β phases, respectively. The overall $[H/M]_{sat}$ presents the sum of the two inputs of the two kinds of receptor sites: $[H/M]_{sat} = [H/M]_{1sat} + [H/M]_{2sat}$. The evolution of $[H/M]_{1sat}$ and $[H/M]_{2sat}$ against temperature for both processes is depicted in Fig. 6.

According to the variation of this parameter, it is clear that the increment of temperature causes the decrease of $[H/M]_{1sat}$ and $[H/M]_{2sat}$, thus the decrease of $[H/M]_{sat}$ affirms the exothermic character of absorption.

Fig. 7 depicts the evolution of the overall saturation absorption quantities of all the studied materials at $T = 243$ K. Obviously, the hydrogen storage capacity of each sample containing RE increases and the La additive-based metal reaches the most elevated capacity. Returning to the values of $[H/M]_{sat}$ determined by the numerical simulation summarized in Table 4, we have noticed that adding Ce, Ho and La leads to the increase of hydrogen absorption amount from 1.65 wt% to 1.67 wt%, 1.68 wt% and 1.76 wt%, respectively, at $T = 243$ K. Whereas, the experimental values of $[H/M]_{sat}$ presented in Table 2 vary from 1.621 wt% to 1.629 wt%, 1.663 wt% and 1.715 wt% for Ce, Ho and La, respectively. The prospective cause for these ameliorated characteristics is the interfacial effect due to RE addition. As RE additives disseminated excellently at the elevated density interface, which supplied the canal for the distribution of H-atoms and ameliorated the performance of hydrogen absorption.[37,60] The rise of the unit cell volume is also another reason providing more locations for hydrogen to reside in.

5.2 Energetic parameters: absorption/desorption energies

Based on the energetic parameters P_1 and P_2 evaluated by fitting the measured isotherms with the chosen model, we calculate the absorption/desorption energies given by the following relations:[61]

$$\Delta E_1 = RT \ln \frac{P_{vs}}{P_1} \quad (19)$$

$$\Delta E_2 = RT \ln \frac{P_{vs}}{P_2} \quad (20)$$

where P_{vs} is the hydrogen saturated vapor pressure and R is the perfect gas constant $R = 8.314472$ J mol^{-1} K^{-1}.

Table 7 summarizes the absorption/desorption energy values determined at three temperatures for all studied alloys.

Fig. 8 represents the temperature dependence of absorption/desorption energies.

Compared to the RE-free sample, the plateau pressures in the RE-containing samples become smaller because of the rise of unit cell volume. The bigger the unit cell volume is, the bigger the interstitial size is, and the lower the platform pressure will be. This result is consistent in accordance between unit cell volume and plateau pressure as previously revealed by Lundin *et al.*[62] Hang *et al.*[63] and Chen *et al.*[64] have also divulged the same results. It is generally accepted that small cell volume results in the decrement of the stability of the metal hydride and has been proven accordingly. Moreover, we have noticed the appearance of a significant fact that the smallest plateau pressure of RE components is related to the biggest atomic number. For example, at $T = 243$ K, Ho (atomic number, 67) provides

Table 7 Values corresponding to the absorption/desorption energies of $Ti_{1.02}Cr_{1.1}Mn_{0.3}Fe_{0.6}RE_{0.03}$ metals at different temperatures

		Absorption		Desorption	
System	T (K)	ΔE_1 (kJ mol^{-1})	ΔE_1 (kJ mol^{-1})	ΔE_1 (kJ mol^{-1})	ΔE_1 (kJ mol^{-1})
$Ti_{1.02}Cr_{1.1}Mn_{0.3}Fe_{0.6}$	243 K	71.286	70.964	72.382	71.158
	253 K	77.595	77.142	78.090	77.219
	263 K	83.897	83.714	84.457	84.067
$Ti_{1.02}Cr_{1.1}Mn_{0.3}Fe_{0.6}La_{0.06}$	243 K	71.018	70.289	72.444	71.158
	253 K	77.072	76.805	78.181	77.154
	263 K	83.936	83.513	84.537	84.129
$Ti_{1.02}Cr_{1.1}Mn_{0.3}Fe_{0.6}Ce_{0.06}$	243 K	72.417	71.707	73.228	73.117
	253 K	78.428	77.605	79.403	78.865
	263 K	84.981	84.079	85.308	85.055
$Ti_{1.02}Cr_{1.1}Mn_{0.3}Fe_{0.6}Ho_{0.06}$	243 K	72.688	72.042	73.443	72.596
	253 K	78.923	77.867	79.513	78.968
	263 K	85.212	84.325	86.968	85.341

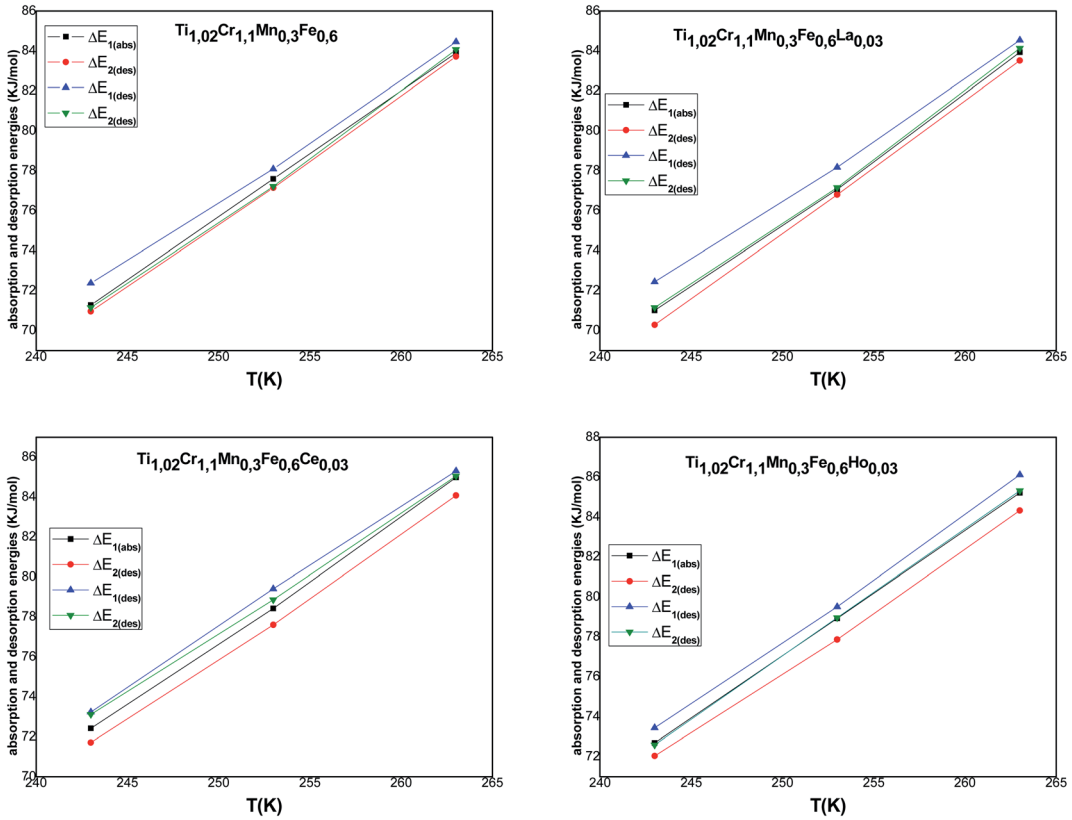

Fig. 8 Evolution of the absorption and desorption energies according to temperature.

hydrogen desorption pressure during α and β phases of $P_1^{'} = 4.46$ MPa and $P_2^{'} = 5.28$ MPa while Ce (atomic number, 58) provides $P_1^{'} = 4.96$ MPa and $P_2^{'} = 5.79$ MPa. Both of them are smaller compared to the release plateau pressure of the RE-free sample at $T = 243$ K, 253 K and 263 K. On the one hand, the absorption/desorption pressures P_1 and P_2 of the four samples increase with the rise of temperature due to the low stabilization of hydrides at elevated temperatures. On the other hand, the hysteresis phenomenon observed in the studied isotherms permits H-atoms to be inserted at a specific pressure plateau but dis-inserted at a lower pressure plateau with absorption.[65] This is certainly due to a relaxation process that minimizes the energy of the site and increases chemical binding.

Concerning the calculated energies related to the equilibrium pressures (Table 7), we can note that the absorption energies ranged from 70 kJ mol^{-1} to 85 kJ mol^{-1} and the desorption energies ranged from 72 kJ mol^{-1} to 86 kJ mol^{-1}. These values indicated that the interaction between hydrogen and metal occurred by chemical absorption (chemisorption). The absorption/desorption energies at each site for the tested alloys are very close to each other. Besides, we can observe that the absorption energy of the first site α is superior to the second: $|\Delta E_2| < |\Delta E_1|$. This behavior can be attributed to the dislocation density occurring at the end of the α phase, which is sufficient to assist both the creation, additionally, during the phase β, the appearance of the migration of incoherent surface. This requires just a few of the dislocation rearrangement, which has appeared and that requires less energy during the β phase.[65,66] It is obvious that the modulus of the released energy is greater than the absorbed energy for all the tested alloys. This is due to the excess energy required to accommodate the restrictions correlated to the expansion volume during the hydride distortion after the hysteresis effect.[67]

6 Thermodynamic interpretation

Thermodynamic potential functions are studied by utilizing the analytical expression related to the appropriate model or more clearly on its partition function. These functions are macroscopic characteristics of the sorption phenomenon. Entropy, internal energy and Gibbs free enthalpy are instances of the macroscopic description of the process.

6.1 Entropy

The entropy is associated with the grand potential through the following expressions:[68,69]

$$J = -k_B T \ln Z_{gc} \quad (21)$$

$$J = -\frac{\partial}{\partial \beta} \ln Z_{gc} - TS_a \quad (22)$$

Then, the entropy can be obtained by:

$$S_a = -\beta k_B \frac{\partial \ln Z_{gc}}{\partial \beta} + k_B \ln Z_{gc} \quad (23)$$

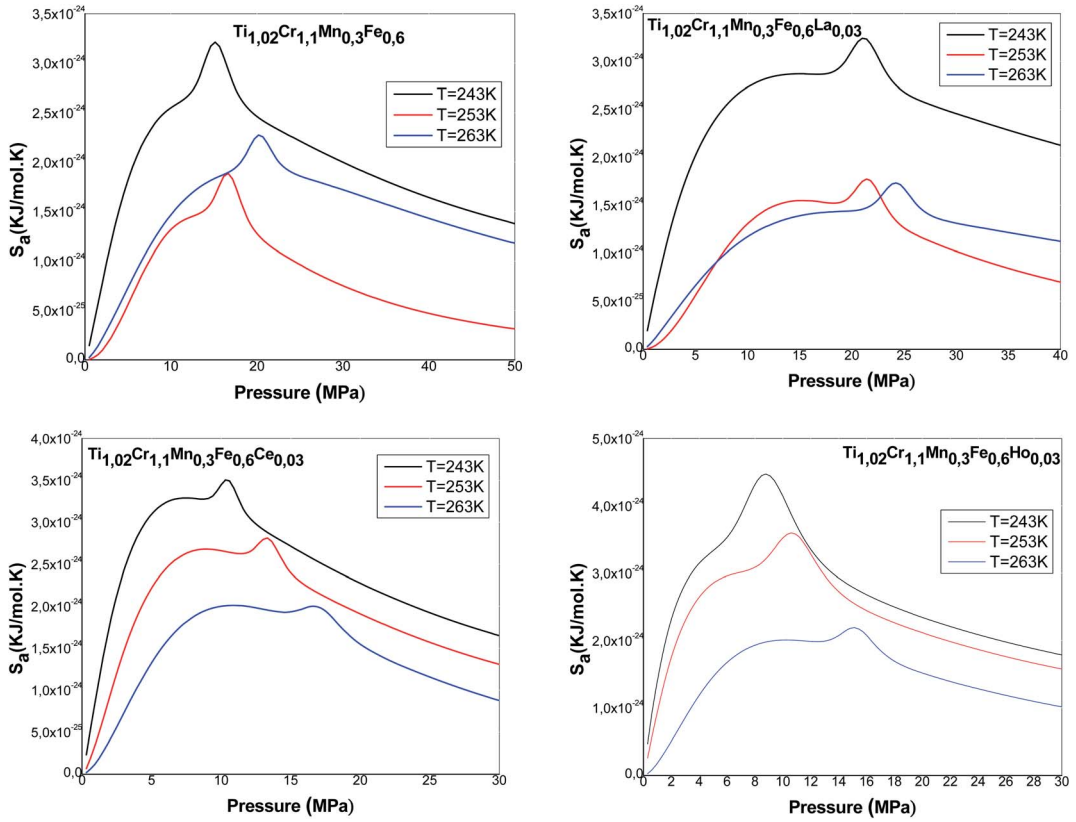

Fig. 9 Evolution of absorption entropy *versus* pressure.

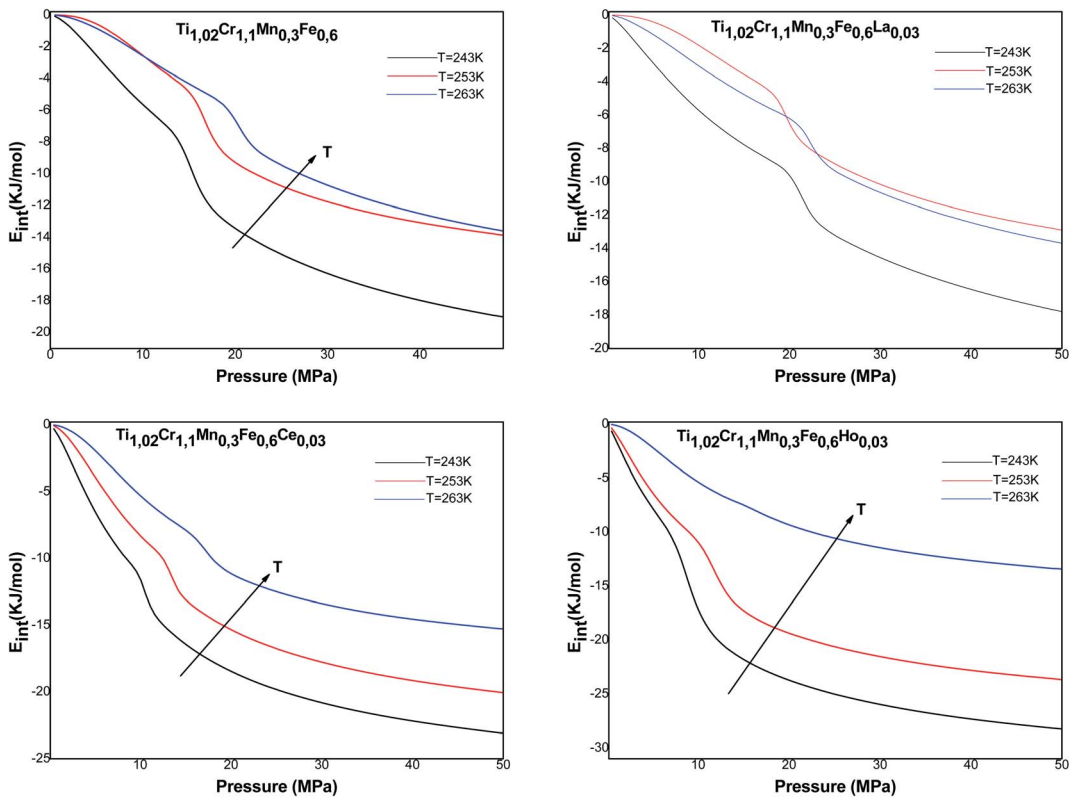

Fig. 10 Evolution of the internal energy *versus* pressure at absorption process.

Depending on the chosen model and utilizing the grand canonical partition function, the statistical entropy S_a is obtained as follow:

$$S_a = k_B \times \left[N_{1m} \ln\left(1 + \left(\frac{P}{P_1}\right)^{n_1}\right) + N_{2m} \ln\left(1 + \left(\frac{P}{P_2}\right)^{n_2}\right) - \left\{ \frac{N_{1m} \times \left(\frac{P}{P_1}\right)^{n_1} \times \ln\left(\frac{P}{P_1}\right)^{n_1}}{\left(1 + \left(\frac{P}{P_1}\right)^{n_1}\right)} + \frac{N_{2m} \times \left(\frac{P}{P_2}\right)^{n_2} \times \ln\left(\frac{P}{P_2}\right)^{n_2}}{\left(1 + \left(\frac{P}{P_2}\right)^{n_2}\right)} \right\} \right] = S_{a1} + S_{a2} \quad (24)$$

Fig. 9 presents the entropy evolution *versus* pressure at various temperatures for all the studied alloys. We note that the entropy presents an almost identical form for all the alloys. It is clearly shown that the entropy is composed mainly of two maxima, revolved around values related to the halves-saturation pressures of α and β sites. Regarding both maxima, the entropy presents two behaviors below and above P_1 and P_2. Actually, the entropy S_{a1} defining the phase α increases at low pressure and achieves a maximum in the proximity of P_1. This can be attributed to the various possibilities of the atoms to pick a free site amongst N_{1m} host sites. These several potentials rise with pressure until a maximum at P_1. After P_1, the entropy gradually decreases due to the reduction in the number of α-free sites and the accessible state's number becomes relatively limited. Then, the entropy S_{a2} corresponding to the phase β starts to rise and to attain, at $P = P_2$, the second maximum. At elevated pressure, atoms have a low possibility to pick a free host site since the alloy tends toward the saturated state and consequently tends toward the order. When the saturated state is completely accomplished, the entropy attains a zero value.

Moreover, we observe that at an appointed pressure, the greater the temperature is, the lower the disorder is. We can also notice that the interstitial site densities decrease with temperature (Fig. 5), thereby there is a decrease in entropy.

6.2 Internal energy

The internal energy is written as follow:[68]

$$E_{int} = -\frac{\partial \ln Z_{gc}}{\partial \beta} + \frac{\mu}{\beta}\left(\frac{\partial \ln Z_{gc}}{\partial \mu}\right) \quad (25)$$

with

$$\mu = k_B T \ln \frac{\beta P}{z_g}$$

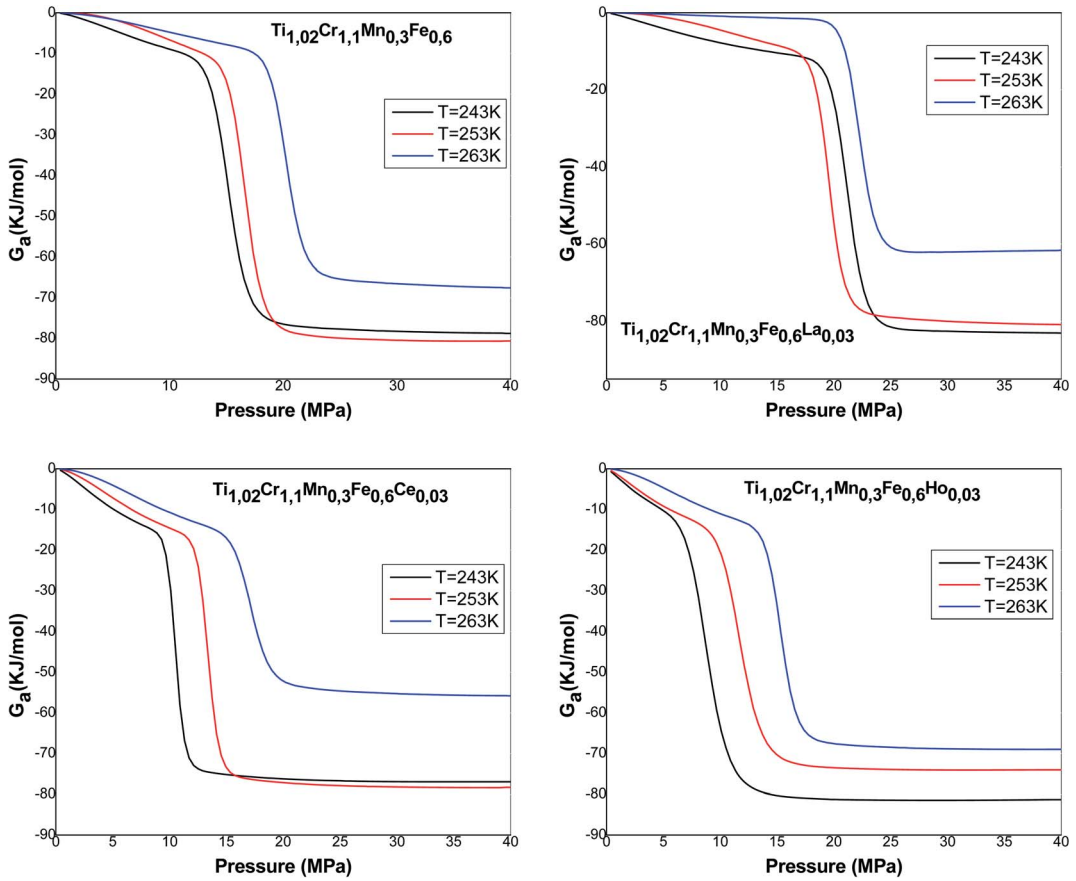

Fig. 11 Evolution of the free enthalpy *versus* pressure at absorption process.

$$z_g = z_{gtr} \times z_{grot} = V\left(\frac{2\pi m k_B T}{h^2}\right)^{3/2} \times \frac{T}{2\theta_{rot}}$$

Thus, we obtain the expression of the internal energy:

$$E_{int} = k_B T \ln\frac{\beta P}{Z_g}\left\{\left(\frac{N_{1m}\left(\frac{P}{P_1}\right)^{n_1}}{\left(1+\left(\frac{P}{P_1}\right)^{n_1}\right)} + \frac{N_{2m}\left(\frac{P}{P_2}\right)^{n_2}}{\left(1+\left(\frac{P}{P_2}\right)^{n_2}\right)}\right)\right\}$$

$$-k_B T\left\{\left(\frac{N_{1m}\left(\frac{P}{P_1}\right)^{n_1}\ln\left(\frac{P}{P_1}\right)^{n_1}}{\left(1+\left(\frac{P}{P_1}\right)^{n_1}\right)} + \frac{N_{2m}\left(\frac{P}{P_2}\right)^{n_2}\ln\left(\frac{P}{P_2}\right)^{n_2}}{\left(1+\left(\frac{P}{P_2}\right)^{n_2}\right)}\right)\right\} \quad (26)$$

The variation of the internal energy *versus* pressure is depicted in Fig. 10. Based on this figure, we observed that the values of E_{int} are negative for the treated alloys at various temperatures. Therefore, during absorption, the alloys release energy, from which the exothermic character of the phenomenon arises.

The increase in temperature, at a fixed pressure, leads to an increase of E_{int} algebraically although there is a decrease in absolute values due to thermal agitation. At high pressure, ΔE_{int} tenders to be zero and therefore E_{int} tenders to limit values, which disclose the saturation state.

6.3 Gibbs free energy

The Gibbs free energy is given by following equation[68]

$$G_a = \mu n N_0 = \mu Q_0 \quad (27)$$

Thus, the obtained expression of G_a is:

$$G_a = k_B T \ln\frac{\beta P}{Z_g}\left(\frac{n_1 N_{1m}}{1+\left(\frac{P_1}{P}\right)^{n_1}} + \frac{n_2 N_{2m}}{1+\left(\frac{P_2}{P}\right)^{n_2}}\right) \quad (28)$$

Fig. 11 presents the Gibbs free energy evolution *versus* pressure. The negative values of G_a indicate that the absorption phenomenon is thermodynamically spontaneous in nature. The Gibbs free energy values increase with the rise of temperature, which shows a lowering of absorption possibility at elevated temperature. The temperature prevents the absorption mechanism to be accomplished.

7 Conclusion

The hydrogen absorption/desorption equilibrium for $Ti_{1.02}Cr_{1.1}Mn_{0.3}Fe_{0.6}RE_{0.03}$ (RE = La, Ce, Ho) metals has been experimentally and theoretically analyzed to reveal the RE adding effect on hydrogen storage and to analyze the absorption/desorption processes. The crystallographic properties and hydrogen storage characteristics of the tested metals were interpreted. The investigation has revealed that all the metals present a gray phase structure defining the C14-type Laves phase and a certain particle phase that is specified like RE oxides. The RE additives in $Ti_{1.02}Cr_{1.1}Mn_{0.3}Fe_{0.6}RE_{0.03}$ metals extend the unit cell and raise the hydrogen storage amount. However, it reduces the absorption/desorption platform pressure of hydrogen.

The monolayer model with two energies is in good accordance with the measured isotherms for all the alloys. The behavior of the adjusted parameters indicated that the hydrogen absorption occurred in a multi-atom manner. The study of the receptor site density indicates that the rise of temperature results in the filling of the host sites. We concluded then that the number of active sites N_m valid for H atoms is generally reduced as a function of temperature. The magnitudes of the calculated absorption/desorption energies show that the hydrogen atoms are chemisorbed on $Ti_{1.02}Cr_{1.1}Mn_{0.3}Fe_{0.6}RE_{0.03}$ alloys. The thermodynamic potential functions have shown that hydrogen absorption was spontaneous and exothermic. The outcome of configurational entropy presented two maxima of disorder at half-saturation pressures.

Conflicts of interest

There are no conflicts to declare.

Acknowledgements

This research was funded by the Deanship of Scientific Research at Princess Nourah bint Abdulrahman University through the Fast-track Research Funding Program to support publication in the top journal (Grant no. 42-FTTJ-02).

References

1 H. C. Lin, K. M. Lin, K. C. Wu, H. H. Hsiung and H. K. Tsai, Cyclic hydrogen absorption-desorption characteristics of TiCrV and $Ti_{08}Cr_{1.2}V$ alloys, *Int. J. Hydrogen Energy*, 2007, **32**, 4966–4972.

2 H. Zhou, H. Z. Liu, L. Xu, S. C. Gao, X. H. Wang and M. Yan, Hydrogen storage properties of Nb-compounds-catalyzed $LiBH_4$–MgH_2, *Rare Met.*, 2017, **36**, 723–728.

3 Z. M. Yuan, W. Zhang, P. L. Zhang, Y. H. Zhang, W. G. Bu, S. H. Guo, *et al.*, Improvement in the hydrogen storage performance of the as-milled Sm-Mg alloys using MoS_2 nano-particle catalysts, *RSC Adv.*, 2017, **7**, 56365–56374.

4 Y. Yin, B. Li, Z. M. Yuan, Y. Qi and Y. H. Zhang, A comparison of TiF_3 and NbF_5 catalytic effects on hydrogen absorption and desorption kinetics of a ball-milled $Mg_{85}Zn_5Ni_{10}$ alloy, *RSC Adv.*, 2018, **8**, 34525–34535.

5 N. A. A. Rusman and M. Dahari, A review on the current progress of metal hydrides material for solid-state hydrogen storage applications, *Int. J. Hydrogen Energy*, 2016, **41**, 12108–12126.

6 Y. Zhang, *et al.*, Development and application of hydrogen storage, *J. Iron Steel Res. Int.*, 2015, **22**, 757–770.

7 B. Zhang and Y. Wu, Recent advances in improving performances of the lightweight complex hydrides Li-MgN-H system, *Prog. Nat. Sci.: Mater. Int.*, 2017, **27**, 21–33.
8 S. Niaz, T. Manzoor and A. H. Pandith, Hydrogen storage: materials, methods and perspectives, *Renewable Sustainable Energy Rev.*, 2015, **50**, 457–469.
9 R. Prabhukhot, M. M. Wagh and A. C. Gangal, A review on solid state hydrogen storage material, *Adv. Energy Power*, 2016, **4**, 11–22.
10 Y. Jia, *et al.*, Combination of nanosizing and interfacial effect: future perspective for designing Mg-based nanomaterials for hydrogen storage, *Renewable Sustainable Energy Rev.*, 2015, **44**, 289–303.
11 A. Eftekhari and B. Fang, Electrochemical hydrogen storage: opportunities for fuel storage, batteries, fuel cells, and supercapacitors, *Int. J. Hydrogen Energy*, 2017, **42**, 25143–25165.
12 C. J. Webb, A review of catalyst-enhanced magnesium hydride as a hydrogen storage material, *J. Phys. Chem. Solids*, 2015, **84**, 96–106.
13 H. Yamada, Electronic structure and magnetic properties of the cubic laves phase transition metal compound, *Phys. B*, 1988, **149**, 390–402.
14 X. Q. Chen, W. Wolf, R. Podloucky and P. Rogl, Ab initio study of ground state properties of the Laves phase compounds. $TiCr_2$, $ZrCr_2$, and $HfCr_2$, *Phys. Rev. B: Condens. Matter Mater. Phys.*, 2005, **71**, 174101.
15 S. B. Gesari, M. E. Pronsato, A. Visintin and A. Juan, Hydrogen storage in AB_2 Laves phase (A = Zr, Ti; B = Ni, Mn, Cr, V): binding energy and electronic structure, *J. Phys. Chem. C*, 2010, **114**, 16832–16836.
16 M. Guo and E. Wu, Thermodynamics of hydrogenation for $Ti_{1-x}Zr_xMnCr$ Laves phase alloys, *J. Alloys Compd.*, 2008, **455**, 191–196.
17 Z. Cao, L. Ouyang, H. Wang, J. Liu, D. Sun, Q. Zhang and M. Zhu, Advanced high pressure metal hydride fabricated *via* Ti-Cr-Mn alloys for hybrid tank, *Int. J. Hydrogen Energy*, 2015, **40**, 2717–2728.
18 S. N. Klyamkin, A. Y. Kovriga and V. N. Verbetsky, Effect of substitution on F.C.C. and B.C.C. hydride phase formation in the $TiCr_2$-H_2 system, *Int. J. Hydrogen Energy*, 1999, **24**, 149–152.
19 J. G. Park, H. Y. Jang, S. C. Han, P. S. Lee and J. Y. Lee, The thermodynamic properties of Ti-Zr-Cr-Mn Laves phase alloys, *J. Alloys Compd.*, 2001, **325**, 293–298.
20 O. Beeri, D. Cohen, Z. Gavra and M. H. Mintz, Sites occupation and thermodynamic properties of the $TiCr_{2-x}Mn_x$-H_2 ($0 < x < 1$) system: statistical thermodynamics analysis, *J. Alloys Compd.*, 2003, **352**, 111–122.
21 E. D. Wu, W. H. Li and J. Li, *Int. J. Hydrogen Energy*, 2012, **37**, 1509–1517.
22 V. Bronca, P. Bergman, V. Ghaemmaghami, D. Khatamian and F. D. Manchester, Hydrogen absorption characteristics of an FeTi + misch metal alloy, *J. Less-Common Met.*, 1985, **108**, 313–325.
23 Y. Yan, Y. Chen, H. Liang, X. Zhou, C. Wu and M. Tao, Effect of Ce on the structure and hydrogen storage properties of $V_{55}Ti_{22.5}Cr_{16.1}Fe_{6.4}$, *J. Alloys Compd.*, 2007, **429**, 301–305.
24 C. Wu, Y. Yan, Y. Chen, M. Tao and X. Zheng, Effect of rare earth (RE) elements on V-based hydrogen storage alloys, *Int. J. Hydrogen Energy*, 2008, **33**, 93–97.
25 X. Liu, L. Jiang, Z. Li, Z. Huang and S. Wang, Improve plateau property of $Ti_{32}Cr_{46}V_{22}$ BCC alloy with heat treatment and Ce additive, *J. Alloys Compd.*, 2009, **471**, 36–38.
26 E. M. Borzone, A. Baruj, M. V. Blanco and G. O. Meyer, Dynamic measurements of hydrogen reaction with $LaNi_{5-x}Sn_x$ alloys, *Int. J. Hydrogen Energy*, 2013, **38**, 7335–7343.
27 G. Liu, D. Chen, Y. Wang and K. Yang, Experimental and computational investigations of $LaNi_{5-x}Al_x$ ($x = 0$, 0.25, 0.5, 0.75 and 1.0) tritium-storage alloys, *J. Mater. Sci. Technol.*, 2018, **34**, 1699–1712.
28 X. Hou, R. Hu, Y. Yang, L. Feng and G. Suo, Modification based on internal refinement and external decoration: a powerful strategy for superior thermodynamics and hysteresis of Mg-Ni hydrogen energy storage alloys, *J. Alloys Compd.*, 2018, **766**, 112–122.
29 D. C. Feng, H. Sun, X. T. Wang and Y. H. Zhang, Effect of milling duration on hydrogen storage thermodynamics and kinetics of ball-milled Ce-Mg-Ni-based alloy powders, *J. Iron Steel Res. Int.*, 2018, **25**, 746–754.
30 J. J. Liu, S. Zhu, Z. Zheng, H. H. Cheng, K. Yan and Z. D. Zhu, Long-term hydrogen absorption/desorption properties and structural changes of $LaNi_4Co$ alloy with double desorption plateaus, *J. Alloys Compd.*, 2019, **778**, 681–690.
31 V. Yartys and R. Denys, Structure properties relationship in $RE_{3-x}Mg_xNi_9H_{10-13}$ (RE = La, Pr, Nd) hydrides for energy storage, *J. Alloys Compd.*, 2015, **645**, 412–418.
32 M. Spodaryk, L. Shcherbakova, A. Sameljuk, A. Wichser, V. Zakaznova-Herzog, M. Holzer, B. Braem, O. Khyzhun, P. Mauron, A. Remhof, Y. Solonin and A. Züttel, Description of the capacity degradation mechanism in $LaNi_5$-based alloy electrodes, *J. Alloys Compd.*, 2015, **621**, 225–231.
33 E. R. Pinatel, M. Palumbo, F. Massimino, P. Rizzi and M. Baricco, Hydrogen sorption in the $LaNi_{5-x}Al_x$-H system ($0 < x < 1$), *Intermetallics*, 2015, **62**, 7–16.
34 M. Ben Yahia, S. Knani, H. Dhaou, M. A. Hachicha, A. Jemni and A. Ben Lamine, Modeling and interpretations by the statistical physics formalism of hydrogen adsorption isotherm on $LaNi_{4.75}Fe_{0.25}$, *Int. J. Hydrogen Energy*, 2013, **38**, 536–542.
35 S. Wjihi, M. Bouzid, L. Sellaoui, S. Knani and H. Dhaoui, Statistical physics modeling of hydrogen sorption onto $LaNi_{4.75}Fe_{0.25}$: microscopic interpretation and thermodynamic potential investigation, *Fluid Phase Equilib.*, 2016, **414**, 170–181.
36 J. Blahovec and S. Yanniotis, Modified classification of sorption isotherms, *J. Food Eng.*, 2009, **91**, 72–77.
37 Z. Yao, L. Liu, X. Xiao, C. Wang, L. Jiang and L. Chen, Effect of rare earth doping on the hydrogen storage performance of

$Ti_{1.02}Cr_{1.1}Mn_{0.3}Fe_{0.6}$ alloy for hybrid hydrogen storage application, *J. Alloys Compd.*, 2018, **731**, 524–530.

38 T. Chi, *Adsorption calculation and modeling*, New York 2, 1994.

39 I. Richard, *Massel Principe's of adsorption and reaction on solid surface*, Urbana, Illinois, 1951, p. 110.

40 S. Wjihi, L. Sellaoui, M. Bouzid, H. Dhaou, S. Knani, A. Jemni, *et al.*, Theoretical study of hydrogen sorption on $LaNi_5$ using statistical physics treatment: microscopic and macroscopic investigation, *Int. J. Hydrogen Energy*, 2017, **42**, 2699–2712.

41 S. Brunauer, P. H. Emmet and E. Teller, Adsorption of gases in multimolecular layers, *J. Am. Chem. Soc.*, 1938, **60**, 309–319.

42 J. Rouquerol, D. Avnir, C. W. Fairbridge and D. H. Everett, Recommendations for the characterization of porous solids, *Pure Appl. Chem.*, 1994, **66**, 1739–1758.

43 A. Ben Lamine and Y. Bouazra, Application of statistical thermodynamics to the olfaction mechanism, *Chem. Senses*, 1997, **22**, 67.

44 L. Sellaoui, D. I. Mendoza-Castillo, H. E. Reynel-Ávila, A. Bonilla-Petriciolet, A. Ben Lamine and A. Erto, A new statistical physics model for the ternary adsorption of Cu^{2+}, Cd^{3+} and Zn^{2+} ions on bone char: Experimental investigation and simulations, *Chem. Eng. J.*, 2018, **343**, 544–553.

45 R. A. Swalin, *Thermodynamics of solids*, John Wiley & Sons, New York, 1962.

46 S. Knani, M. Mathlouthi and A. Ben Lamine, Modeling of the psychophysical response curves using the grand canonical ensemble in statistical physics, *Food Biophys.*, 2007, **2**, 183–192.

47 N. Bouaziz, M. Ben Manaa and A. Ben Lamine, Theoretical study of hydrogen absorption-desorption on $LaNi_{3.8}Al_{1.2-x}Mn_x$ using statistical physics treatment, *Phys. B*, 2017, **525**, 46–59.

48 S. Knani, F. Aouainia, N. Bahloul, M. Khalfaoui, M. A. Hachicha, A. Ben Lamine, *et al.*, Modeling of adsorption isotherms of water vapor on Tunisian olive leaves using statistical mechanical formulation, *Phys. A*, 2014, **400**, 57–70.

49 B. Diu, C. Guthmann, D. Lederer and B. Roulet, *Physique Statistique*, Hermann, Paris, 1989.

50 C. Tien, Adsorption calculations and modeling, in *Series in chemical engineering*, Butterworth-Heinemann, London, 1994.

51 J. Li and C. J. Werth, Modeling sorption isotherms of volatile organic chemical mixtures in model and natural solids, *Environ. Toxicol. Chem.*, 2002, **21**, 1377–1383.

52 S. Wjihi, C. Briki, L. Sellaoui, A. Jemni and A. Ben Lamine, Theoretical study of hydrogen desorption on $Mg_{50}Ni_{50}$ using statistical physics treatment, *Int. J. Hydrogen Energy*, 2016, **42**, 8733–8743.

53 D. W. Marquardt, An algorithmfor least-squares estimation of nonlinear parameters, *J. Soc. Ind. Appl. Math.*, 1963, **11**, 431–441.

54 A. Kapoor and R. T. Yang, Correlation of equilibrium adsorption data of condensable vapours on porous adsorbents, *Gas Sep. Purif.*, 1989, **3**, 187–192.

55 D. P. Shoemaker and C. B. Shoemaker, Concerning atomic sites and capacities for hydrogen absorption in the AB_2 Friauf-Laves phases, *J. Less-Common Met.*, 1979, **68**, 43–58.

56 R. G. Agostino, G. Liberti, V. Formoso and E. Colavita, *In situ* X-ray absorption study of $Zr(V_{0.29}Ni_{0.71})_3$ hydride electrodes, *Phys. Rev. B: Condens. Matter Mater. Phys.*, 2000, **61**, 13647–13648.

57 S. Hong and C. L. Fu, Hydrogen in Laves phase ZrX_2 (X = V, Cr, Mn, Fe, Co, Ni) compounds: binding energies and electronic and magnetic structure, *Phys. Rev. B: Condens. Matter Mater. Phys.*, 2002, **66**, 094109.

58 S. B. Gesari, M. E. Pronsato, A. Visintin and A. Juan, Hydrogen storage in AB_2 laves phase (A = Zr, Ti; B = Ni, Mn, Cr, V): binding energy and electronic structure, *J. Phys. Chem.*, 2010, **114**, 16832–16836.

59 Y. Anikina and V. N. Verbetsky, Calorimetric investigation of the hydrogen interaction with $Ti_{0.9}Zr_{0.1}Mn_{1.2}V_{0.1}$, *Int. J. Hydrogen Energy*, 2011, **36**, 1344–1348.

60 X. Liu, L. Jiang, Z. Li, Z. Huang and S. Wang, Improve plateau property of $Ti_{32}Cr_{46}V_{22}$ BCC alloy with heat treatment and Ce additive, *J. Alloys Compd.*, 2009, **471**, 36e38.

61 N. Bouaziz, M. Bouzid and A. Ben Lamine, Theoretical study of hydrogen absorption and desorption in $Ti_{1-x}Zr_xMn_{1.4}$ using statistical physics treatment: Microscopic investigation and thermodynamic potential interpretation, *Int. J. Hydrogen Energy*, 2018, **43**, 1615–1633.

62 C. Lundin, F. Lynch and C. Magee, A correlation between the interstitial hole sizes in intermetallic compounds and the thermodynamic properties of the hydrides formed from those compounds, *J. Less-Common Met.*, 1977, **56**, 19–37.

63 Z. Hang, L. Chen, X. Xiao, S. Li, C. Chen, Y. Lei and Q. Wang, The effect of Cr content on the structural and hydrogen storage characteristics of $Ti_{10}V_{80-x}Fe_6Zr_4Cr_x$ (x = 0–14) alloys, *J. Alloys Compd.*, 2010, **493**, 396–400.

64 Z. Chen, X. Xiao, L. Chen, X. Fan, L. Liu, S. Li, H. Ge and Q. Wang, Influence of Ti super-stoichiometry on the hydrogen storage properties of $Ti_{1+x}Cr_{1.2}Mn_{0.2}Fe_{0.6}$ (x = 0–0.1) alloys for hybrid hydrogen storage application, *J. Alloys Compd.*, 2014, **585**, 307–311.

65 P. J. Cappillino, E. J. Lavernia, M. D. Ong, W. G. Wolfer and N. Y. Yang, Plastic deformation and hysteresis for hydrogen storage in Pd-Rh alloys, *J. Alloys Compd.*, 2014, **586**, 59–65.

66 Q. Kong, W. Feng, X. Zhong, Y. Liu and L. Lian, Hydrogen absorption/desorption properties of porous hollow palladium spheres prepared by templating method, *J. Alloys Compd.*, 2016, **664**, 188–192.

67 R. Balasubramaniam, Hysteresis in metal-hydrogen systems, *J. Alloys Compd.*, 1997, **253**, 203–206.

68 L. Couture and R. Zitoun, Physique statistique, *J. Ellipses*, 1992, **524**, 375.

69 K. H. Norwich, Determination of saltiness from the laws of thermodynamics estimating the gas constant from psychophysical experiments, *Chem. Senses*, 2001, **26**, 1015–1022.